

lower-level expression of SAE1 and SAE2 had significantly better metastasis-free survival than those with higher SAE1 and SAE2 (Fig. 4D, left panel, $P = 0.01$ log-rank test). By contrast, lower-level expression of SAE1 and SAE2 did not correlate with outcome in patients with Myc-low tumors (Fig. 4D, right panel). This suggests that Myc hyperactivation leads to an increased dependency on SAE1 and SAE2 in human breast cancers.

We have shown here that the E1 SAE 1 and 2 enable cells to tolerate Myc hyperactivation. SAE1 and SAE2 represent enzymatic examples of the “non-oncogene addiction” concept, and their discovery illustrates the power of unbiased genetic screens for identifying potential new leads for cancer therapeutics. Loss of SUMOylation leads to substantial mitotic catastrophe and cell death by switching a subprogram of Myc transcriptional targets that support mitotic spindle function. Thus, inactivation of SAE2 mimics the mitotic disruption caused by spindle poisons, but in a genotype-specific way (i.e., selectively in cells that harbor oncogenic Myc activation). Notably, mitotic interference is a mainstay of cancer therapeutics, and agents such as taxanes that disrupt proper spindle function are used to treat a wide variety of cancers. However, a major limitation of this class of therapeutics is their toxicity to nontumor organ systems, thus limiting their therapeutic window. Our observation that inhibition of SUMOylation can mimic spindle poisons selectively in cells expressing hyperactivated Myc raises the possibility that drugs targeting the SUMO pathway may have the antitumor effects of spindle poisons with fewer side effects.

Myc promotes a balance of pro- and anti-tumorigenic properties, and mutations in Myc can shift this balance in pro- and anti-oncogenic Myc functions, demonstrating that distinct transcriptional (or other biochemical) functions of Myc may be segregated (15, 16). We propose that the Myc transcriptional program can be shifted to favor the anti-oncogenic state. Specifically, our data suggest that the inactivation of SAE2 drives synthetic lethality with the Myc oncogene by altering a subprogram of Myc transcriptional targets that supports proper mitosis and thus cell viability, a subprogram we term SUMOylation-dependent Myc switchers, or SMS genes. This SMS program is highly enriched in proteins that control spindle integrity, and the Myc-SAE2 synthetic lethal interaction elicits frequent aberrations in the mitotic spindle and eventual cell death. SUMOylation may thus contribute to Myc-induced oncogenesis at least in part by cooperating with Myc to maintain expression of Myc target genes involved in mitotic fidelity. These observations highlight the idea that altering distinct subprograms of Myc transcription (by SAE2 inactivation or other mechanisms) may be exploited as a therapeutic strategy in Myc-driven cancers, and more broadly, suggest that subverting transcriptional programs may be a general strategy in treating cancers driven by oncogenic transcrip-

tion factors that are notoriously difficult to target therapeutically.

References and Notes

1. I. B. Weinstein, *Science* **297**, 63 (2002).
2. S. W. Lowe, E. Cepero, G. Evan, *Nature* **432**, 307 (2004).
3. S. Jones et al., *Science* **321**, 1801 (2008).
4. J. Luo, N. L. Solimini, S. J. Elledge, *Cell* **136**, 823 (2009).
5. P. G. Richardson, C. Mitsiades, T. Hideshima, K. C. Anderson, *Annu. Rev. Med.* **57**, 33 (2006).
6. H. Farmer et al., *Nature* **434**, 917 (2005).
7. L. Soucek, G. I. Evan, *Curr. Opin. Genet. Dev.* **20**, 91 (2010) (Feb).
8. S. L. Deming, S. J. Nass, R. B. Dickson, B. J. Trock, *Br. J. Cancer* **83**, 1688 (2000).
9. M. J. van de Vijver et al., *N. Engl. J. Med.* **347**, 1999 (2005).
10. K. Chin et al., *Cancer Cell* **10**, 529 (2006).
11. A. S. Adler et al., *Nat. Genet.* **38**, 421 (2006).
12. Y. Chen, O. I. Olopade, *Expert Rev. Anticancer Ther.* **8**, 1689 (2008).
13. L. Soucek et al., *Nature* **455**, 679 (2008).
14. R. B. Boxer, J. W. Jang, L. Sintasath, L. A. Chodosh, *Cancer Cell* **6**, 577 (2004).
15. M. T. Hemann et al., *Nature* **436**, 807 (2005).
16. D. W. Chang, G. F. Claassen, S. R. Hann, M. D. Cole, *Mol. Cell. Biol.* **20**, 4309 (2000).
17. A. Menssen et al., *Cell Cycle* **6**, 339 (2007).
18. S. Rottmann, Y. Wang, M. Nasoff, Q. L. Deveraux, K. C. Quon, *Proc. Natl. Acad. Sci. U.S.A.* **102**, 15195 (2005).
19. Y. Wang et al., *Cancer Cell* **5**, 501 (2004).
20. E. A. Beierle et al., *J. Biol. Chem.* **282**, 12503 (2007).
21. F. Zindy et al., *Genes Dev.* **12**, 2424 (1998).
22. O. Vafa et al., *Mol. Cell* **9**, 1031 (2002).
23. H. Hermeking, D. Eick, *Science* **265**, 2091 (1994).
24. R. T. Hay, *Mol. Cell* **18**, 1 (2005).
25. K. L. Meerbrey et al., *Proc. Natl. Acad. Sci. U.S.A.* **108**, 3665 (2011).
26. V. Joukov et al., *Cell* **127**, 539 (2006).
27. L. Song, M. Rape, *Mol. Cell* **38**, 369 (2010).
28. T. Kiyomitsu, C. Obuse, M. Yanagida, *Dev. Cell* **13**, 663 (2007).
29. M. Shuaib, K. Ouararhni, S. Dimitrov, A. Hamiche, *Proc. Natl. Acad. Sci. U.S.A.* **107**, 1349 (2010).
30. J. Higgins et al., *BMC Cell Biol.* **11**, 85 (2010).
31. H. H. Silljé, S. Nagel, R. Körner, E. A. Nigg, *Curr. Biol.* **16**, 731 (2006).
32. S. Loi et al., *Proc. Natl. Acad. Sci. U.S.A.* **107**, 10208 (2010).
33. Y. Wang et al., *Lancet* **365**, 671 (2005).
34. C. Desmedt et al.; TRANSBIG Consortium, *Clin. Cancer Res.* **13**, 3207 (2007).
35. L. D. Miller et al., *Proc. Natl. Acad. Sci. U.S.A.* **102**, 13550 (2005).
36. M. Schmidt et al., *Cancer Res.* **68**, 5405 (2008).
37. Y. Zhang et al., *Breast Cancer Res. Treat.* **116**, 303 (2009).
38. A. J. Minn et al., *Proc. Natl. Acad. Sci. U.S.A.* **104**, 6740 (2007).
39. A. J. Minn et al., *Nature* **436**, 518 (2005).

Acknowledgments: We thank C. Bland for critical comments on the manuscript and T. Mitchell, W. Choi, S. Songyang, and the BCM C-BASS and CCSC Cores for reagents and technical assistance. J.D.K and K.L.M. are supported by NIH training grants T32HD05520/T32CA090221-09 and U.S. Department of Defense predoctoral fellowship W81XWH-10-1-0354, respectively. The Golding lab is supported by NIH grant R01GM082837, Human Frontier Science Program grant RGY70/2008, Welch Foundation grant Q-1759, and NSF grant 082265 (PFC: Center for the Physics of Living Cells). This work was supported by a Susan G. Komen for the Cure grant (KG090355), CPRIT grant (RP120583), and NIH grant (CA149196) to T.F.W., Specialized Program of Research Excellence developmental grant (P50 CA058183) to T.F.W., SU2C–American Association for Cancer Research Breast Cancer program grant to R.S. and C.K.O., and U.S. Army Innovator Award (W81XWH0410197) to S.J.E. S.J.E. is an Investigator with the Howard Hughes Medical Institute. T.F.W. is a scholar of The V Foundation and The Mary Kay Ash Foundation for Cancer Research. Gene Expression data are deposited in GEO (accession no. GSE34055).

Supporting Online Material

www.sciencemag.org/cgi/content/full/science.1212728/DC1
Materials and Methods
Figs. S1 to S14
Tables S1 and S2
References

16 August 2011; accepted 22 November 2011
Published online 8 December 2011;
10.1126/science.1212728

Locally Synchronized Synaptic Inputs

Naoya Takahashi,¹ Kazuo Kitamura,^{2,3} Naoki Matsuo,^{3,4} Mark Mayford,⁵ Masanobu Kano,² Norio Matsuki,¹ Yuji Ikegaya^{1,3*}

Synaptic inputs on dendrites are nonlinearly converted to action potential outputs, yet the spatiotemporal patterns of dendritic activation remain to be elucidated at single-synapse resolution. In rodents, we optically imaged synaptic activities from hundreds of dendritic spines in hippocampal and neocortical pyramidal neurons *ex vivo* and *in vivo*. Adjacent spines were frequently synchronized in spontaneously active networks, thereby forming dendritic foci that received locally convergent inputs from presynaptic cell assemblies. This precise subcellular geometry manifested itself during *N*-methyl-D-aspartate receptor-dependent circuit remodeling. Thus, clustered synaptic plasticity is innately programmed to compartmentalize correlated inputs along dendrites and may reify nonlinear synaptic integration.

Cortical microcircuits are nonrandomly intertwined and form cell assemblies that fire in a spatiotemporally orchestrated manner. This patterned activity is decoded by the dendrites of downstream neurons. Dendrites are arborized and electrically active (*I*), which allows them to exhibit local nonlinear membrane potential dynamics

(2–4) and to transform different spatiotemporal sequences of incoming inputs into different output patterns (5, 6). Therefore, knowing whether synaptic inputs are clustered or dispersed over dendrites at a given time (fig. S1) is critical for determining the dendritic computational power (7, 8); however, these dynamics are still poorly understood.

We monitored spontaneous synaptic inputs using dual patch-clamp recordings under confocal visualization from different apical dendritic

branches of individual CA3 pyramidal cells in rat hippocampal slices that were cultured for 12 to 19 days (fig. S2A) (9). Large postsynaptic potentials (that is, putative synchronized inputs) often occurred in only one branch (fig. S2B). The Euclidean distance in membrane potentials between two branches was distributed with a long tail (fig. S2C), suggesting that dendrites received spatially biased synchronous inputs.

Next, we intracellularly injected CA3 pyramidal cells with Fluo-5F through somatic patch-clamp pipettes (Fig. 1A) (10). We voltage-clamped a neuron at -30 mV and imaged the dendrites in an area of approximately $100 \times 100 \mu\text{m}^2$ that con-

tained an average of 98.5 ± 16.7 spines (mean \pm SD, ranging from 52 to 235 spines) (Fig. 1B). Transient calcium elevations occurred spontaneously in the spines (Fig. 1, C and D, and movie S1). These activities were spatially restricted within the spines (Fig. 1C) and were time-locked to the occurrence of spontaneous excitatory postsynaptic currents (EPSCs) in the patched neurons (fig. S3A). The local application of 1 mM L,D-2-amino-5-phosphonopentanoic acid (AP5), an N-methyl-D-aspartate (NMDA) receptor antagonist, abolished spine calcium events without affecting the overall frequency of the spontaneous EPSCs (fig. S3, B to G). The mean frequency

Fig. 1. Imaging of spontaneous synaptic inputs. (A) A stack image of a CA3 pyramidal cell filled with Fluo-5F. (B) The locations of 137 spines (red) monitored from the boxed region shown in (A). (C) Spontaneous calcium events of spines in the region boxed in (B). $\Delta F/F$, percent increase in fluorescence intensity. (D) The spatiotemporal pattern of the calcium events of the 137 spines. Each dot indicates a single event of a single spine. (E) The event frequencies are plotted versus the path distance from the soma. Each black dot represents a single spine ($n = 1084$ spines in 11 videos from 11 slices). Red dots and bars indicate the means \pm SDs. (F) A Lorenz curve representing the proportion of the total inputs that is assumed by the proportion of spines with the lowest input frequencies. (G) Distributions of the input frequencies and the head sizes of the spines.

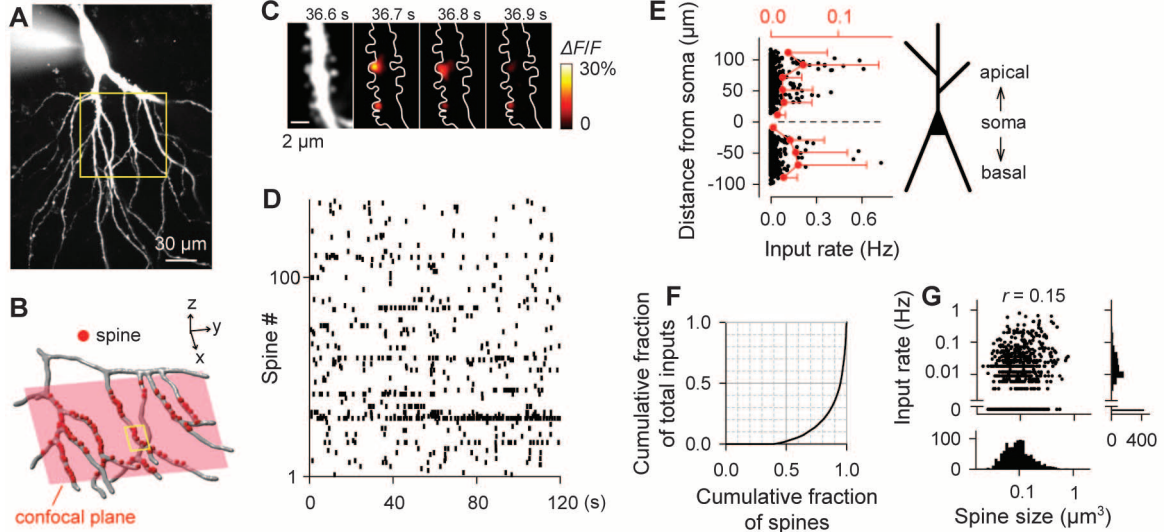
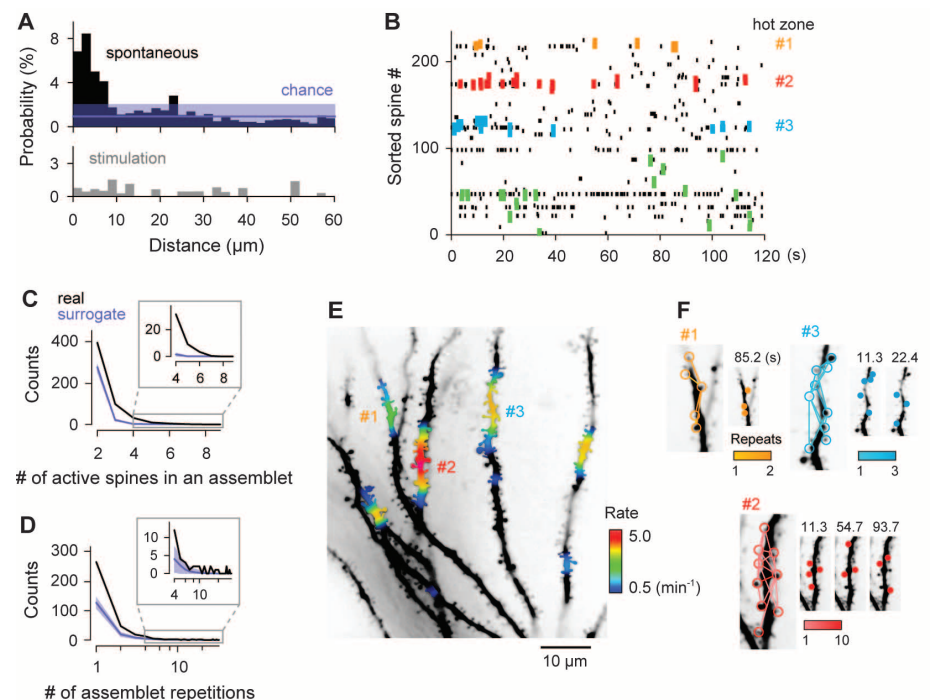


Fig. 2. Functionally clustered spine activity *ex vivo*. (A) (Top) The probability of observing spines coactivated within 100 ms as a function of the distance from a given spine ($n = 11$ videos from 11 neurons). The chance level and its 95% confidence intervals (purple) were estimated from the distribution of distances of more than $10 \mu\text{m}$. (Bottom) Spine coactivation in response to electrical stimulation of the CA3 stratum radiatum ($n = 16$ videos from 10 neurons). (B) Assemblies (thick dots) in a raster plot of 235 spines. Assemblies that appear in hot zones 1, 2, and 3 in (E) are colored in yellow, red, and blue; otherwise, they are colored in green. (C and D) Distribution of the number of spines participating in single assemblies (C) and the repetition numbers of each assembly (D). Chance (purple) was estimated by the random shuffling of inter-event intervals and is represented by the mean value of 1000 surrogates and their 95% confidence intervals. The data from 11 neurons are pooled. (E) A heat map of the frequency of assemblies in dendrites. (F) Representative assembly dynamics in hot zones 1, 2, and 3.



of spine activities was 1.5 events/min, which was approximately half the mean firing rate of the presynaptic neuron population (fig. S4). This difference may result from stochastic synaptic transmission, with a probability of about 50% between CA3 pyramidal cells *ex vivo* (11), as well as from false-negative detection of a fraction of spine calcium events.

The locations of spines were three-dimensionally determined post hoc to measure the path length from the soma along the dendrites. The spines did not differ with respect to activity levels between the basal and radial oblique dendrites or between the proximal and distal dendrites (Fig. 1E). Therefore, all data were pooled in the following analyses. The Gini coefficient of the spine activity was 0.78; approximately 20% of the spines exhibited 80% of the calcium activity (Fig. 1F). The activity frequency and the spine head size, each of which approximated a log-normal distribution, correlated only weakly with each other (Fig. 1G, Spearman's rank $r = 0.15$, $P = 5.9 \times 10^{-7}$).

We calculated the spatial correlations of spontaneous spine activities; for a given activity in a “focused” spine, the probability of observing activity in other spines in a time window of 100 ms was plotted as a function of the path length from the focused spine (Fig. 2A, top; $n =$

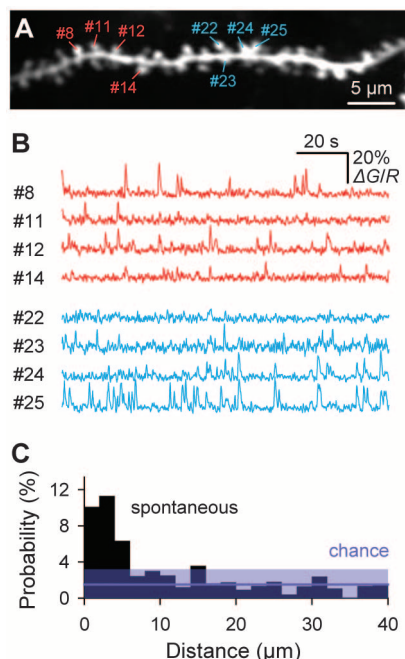


Fig. 3. Functionally clustered spine activity in vivo. **(A)** A stack image of dendrites of an Alexa 594–loaded layer 2/3 pyramidal cell in the mouse somatosensory cortex in vivo. **(B)** Typical traces of spontaneous calcium activity from eight spines shown in **(A)**. **(C)** The probability of observing coactivated spines as a function of the inter-spine path distance ($n = 10$ dendritic segments in four cells). The chance level and its 95% confidence intervals (purple) were estimated from the distribution of distances of more than 10 μm.

11 videos from 11 neurons in 11 slices). The probability was compensated with the spine density observed at a given distance to avoid sampling bias caused by the limited lengths of monitored dendritic segments. Spine coactivation was significantly more frequent within interspine intervals of 8 μm as compared to the chance level, which is defined here as the mean probability of observing spine activity at distances greater than 10 μm ($|Z| \geq 5.77$, $P \leq 8.0 \times 10^{-9}$, Z -test for a population mean). The spatially clustered spine activation was also significant as compared to randomized surrogates (fig. S5A, $P < 0.01$). We did not observe clustered synaptic inputs in fast-spiking parvalbumin-positive interneurons in the CA3 stratum pyramidale (fig. S6, $|Z| \geq 0.63$, $P \leq 0.53$; fig. S5B; $n = 11$ videos from eight neurons).

To examine the synaptic activation patterns in vivo, we conducted somatic whole-cell patch-clamp recordings (12) and two-photon calcium imaging from spines of layer 2/3 pyramidal cells in the barrel cortex of anesthetized young adult mice. Calcium activities were simultaneously monitored from 31.6 ± 13.7 spines (ranging from 16 to 48 spines) from 10 apical or basal dendrites of four cells (Fig. 3, A and B). Spontaneous activities frequently occurred in neighboring spines; the probability of observing the coactive spines significantly increased within 6 μm along the dendrites (Fig. 3C, $|Z| \geq 5.61$, $P \leq 2.1 \times 10^{-8}$; fig. S5C).

The synchronization of adjacent spines can be explained by five possible mechanisms: (i) convergent afferents from a population of spontaneously synchronized presynaptic neurons (cell assembly) (fig. S7A); (ii) multiple innervations of a single presynaptic axon (fig. S7B); (iii) spill-

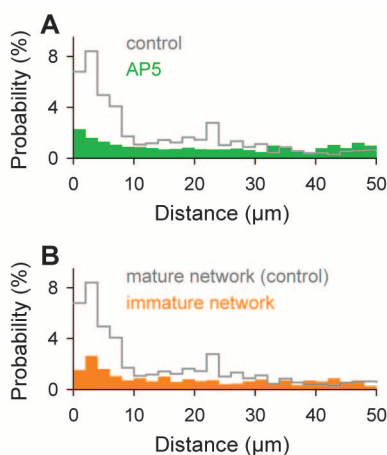


Fig. 4. NMDA receptor–dependent emergence of clustered synaptic inputs. **(A)** The probability of observing coactivated spines as a function of the path distance in slices cultivated in the chronic presence of 100 μM AP5 ($n = 8$ videos from eight neurons). **(B)** The probability of observing coactivated spines in immature networks of slices for 3 to 4 days in vitro ($n = 14$ videos from 14 neurons). Early calcium sparks in immature dendritic shafts were excluded from data analysis. The control is the same as in Fig. 2A.

over of diffusible molecules (such as glutamate) to neighboring synapses (fig. S7C); (iv) spatial segregation of spine excitation by local dendritic inhibition (fig. S7D); or (v) local depolarization-induced increase in a chance of calcium influx in neighboring spines. We can rule out mechanisms ii to v on the basis of the results of the three following experiments *ex vivo*. First, we applied electrical field stimulation to the CA3 stratum radiatum and produced synchronized network activity. The stimulation intensity was set to evoke a compound EPSC with an amplitude greater than 400 pA in the patched neurons. This cell assembly–irrelevant artificial synchronization did not generate spatially clustered spine activation (Fig. 2A, bottom, $|Z| \geq 0.45$, $P \leq 0.65$; fig. S5D; $n = 16$ videos from 10 neurons). This result is inconsistent with ii, iii, and v. Second, we can also rule out mechanism ii because biocytin reconstructions of synaptically connected neurons revealed that 51 of 55 (92.7%) putative synapses arising from 12 presynaptic neurons contacted single spines (fig. S8). Finally, we can exclude mechanism iv because spine activation remained clustered in dendrites that were disinhibited by the local application of 1 mM picrotoxin (fig. S9, $|Z| \geq 3.97$, $P \leq 7.2 \times 10^{-5}$; fig. S5E; $n = 8$ videos from eight neurons). Therefore, mechanism i appeared to be the most plausible mechanism (fig. S1A).

To intuitively depict the observed spine coactivation, we defined an “assembled” as a cluster of synchronized spine activities in which the distance from any spine in the cluster to the next nearest spine in the cluster was less than 10 μm (Fig. 2B). In the entire sample of 11 videos *ex vivo*, 31.5% of the spines participated in at least one assembled, and assembled activity accounted for 29.5% of the total spine activity. In single assembled events, an average of 3.6 ± 0.7 spines, ranging from 2 to 12 spines, were activated during a period of 59 ± 33 ms and within an area of 4.7 ± 3.3 μm (Fig. 2C). Twenty-eight percent of the assemblies appeared more than once, and a portion of them repeated up to 30 times (Fig. 2D), whereas 58.9% of the spines that participated in one assembled participated in other assemblies. The assembled sizes and the numbers of repetitions were greater than the chance values expected by event-interval shuffling (Fig. 2, C and D, purple; $P < 0.001$), in which the time intervals between successive calcium events were randomly exchanged within each spine to collapse the time correlations between spines (13).

In regard to the population dynamics, 85.0% of the assemblies occurred sporadically, whereas the remaining 15.0% occurred in synchrony with other assemblies (fig. S10A). When synchronized, the assemblies tended to appear more than 80 μm apart from one other (fig. S10B).

Dendrites were spatially heterogeneous in emitting assemblies (Fig. 2, E and F). Therefore, we defined a hot zone as a continuous dendritic segment where a single assembled or multiple assemblies that shared at least one spine occurred. The hot zones had an average area of 7.7 ± 6.7 μm,

ranging from 0.4 to 28.2 μm (fig. S11A), and exhibited an average of 2.7 ± 4.8 assemblets/min, ranging from 0.04 to 25.0 assemblets/min (fig. S11B). Hot zones were dispersed at a density of 1.8 ± 1.2 , ranging from 0 to 6, per 50 μm of dendritic length (fig. S11C). They are candidate sites for the initiation of dendritic spikes (14), but we rarely observed calcium sparks in the dendritic shafts, which may possibly be due to a lowered spine density in slice cultures (fig. S13B) as compared to cortical neurons in vivo.

Spines that participated in assemblets were larger in head size than nonparticipants (fig. S12), which suggests that assemblets are shaped by long-term synaptic plasticity (15). Indeed, adjacent spines were less synchronized in slices cultivated in the presence of 100 μM AP5 for 12 to 19 days (Fig. 4A, $|Z| \geq 1.05$, $P \leq 0.30$; fig. S5F; $n = 8$ videos from 8 neurons) and in immature slices cultivated for 3 to 4 days (Fig. 4B, $|Z| \geq 1.51$, $P \leq 0.13$; fig. S5G; $n = 14$ videos from 14 neurons) as compared to control mature slices ($P < 0.01$ each; Kolmogorov-Smirnov test). Neither the spine density nor the spontaneous or miniature EPSC levels differed between control and AP5-treated cultures (fig. S13). Thus, functional synaptic clustering is likely to develop through NMDA receptor-dependent circuit remodeling.

Consistent with this idea, we found that glutamate receptors were preferentially inserted into neighboring spines after behavioral exploration in vivo, using adult transgenic mice in which GFP-GluR1 is expressed under control of the *c-fos* promoter (figs. S5H and S14) (16). Thus, the loci of synaptic plasticity are spatially clustered over dendrites. The clustered plasticity may result from interspine interactions that heterosynaptically modulate the threshold for long-term potentiation, such as local depolarization-induced Mg^{2+} unblock of nearby NMDA receptors or intracellular diffusion of plasticity-associated molecules (17–20).

We found that synaptic inputs were frequently synchronized within a group of spines in the im-

mediate vicinity of one another. Given that ex vivo networks are subject to massive axon reorganization during cultivation without external inputs, our data indicate that the locally convergent connectivity that generates assemblets emerges through self-organization (fig. S15). Thus, the default principle for designing circuit topology is biased to facilitate dendritic compartmentalization (21). The resultant clustered synchrony may offer opportunities for associative learning, because vicinal spines encode different information (22, 23).

Because the video frame rate of our spine imaging was limited to a maximum of 20 Hz to maintain the signal-to-noise ratio, we could not determine the internal structure of assemblets; however, given that the ex vivo hippocampal network synchrony accompanies sharp waves and ripples (24), assemblets are expected to coordinate temporal activity sequences (25). Such sequential activation would facilitate nonlinear synaptic integration and enhance the computational power of a single neuron (5).

Note added in proof: Two recent studies have reported phenomena partly related to those described here, demonstrating activity-dependent clustering of synaptic inputs to developing dendrites of hippocampal slice cultures (26) and clustered synaptic plasticity in the developing somatosensory cortex (27).

References and Notes

- M. London, M. Häusser, *Annu. Rev. Neurosci.* **28**, 503 (2005).
- J. Schiller, Y. Schiller, G. Stuart, B. Sakmann, *J. Physiol.* **505**, 605 (1997).
- N. L. Golding, N. Spruston, *Neuron* **21**, 1189 (1998).
- J. Schiller, G. Major, H. J. Koester, Y. Schiller, *Nature* **404**, 285 (2000).
- T. Branco, B. A. Clark, M. Häusser, *Science* **329**, 1671 (2010).
- M. E. Larkum, J. J. Zhu, B. Sakmann, *Nature* **398**, 338 (1999).
- M. Häusser, B. Mel, *Curr. Opin. Neurobiol.* **13**, 372 (2003).
- A. Losonczy, J. C. Magee, *Neuron* **50**, 291 (2006).

- T. Sasaki, N. Matsuki, Y. Ikegaya, *Science* **331**, 599 (2011).
- Materials and methods are available as supporting material on Science Online.
- J. M. Montgomery, P. Pavlidis, D. V. Madison, *Neuron* **29**, 691 (2001).
- K. Kitamura, B. Judkewitz, M. Kano, W. Denk, M. Häusser, *Nat. Methods* **5**, 61 (2008).
- Y. Ikegaya et al., *Science* **304**, 559 (2004).
- S. Gasparini, M. Migliore, J. C. Magee, *J. Neurosci.* **24**, 11046 (2004).
- M. Matsuzaki, N. Honkura, G. C. Ellis-Davies, H. Kasai, *Nature* **429**, 761 (2004).
- N. Matsuo, L. Reijmers, M. Mayford, *Science* **319**, 1104 (2008).
- C. D. Harvey, K. Svoboda, *Nature* **450**, 1195 (2007).
- C. D. Harvey, R. Yasuda, H. Zhong, K. Svoboda, *Science* **321**, 136 (2008).
- A. Losonczy, J. K. Makara, J. C. Magee, *Nature* **452**, 436 (2008).
- A. Govindarajan, I. Israely, S. Y. Huang, S. Tonegawa, *Neuron* **69**, 132 (2011).
- W. M. DeBello, *Trends Neurosci.* **31**, 577 (2008).
- X. Chen, U. Leischner, N. L. Rochefort, I. Nelken, A. Konnerth, *Nature* **475**, 501 (2011).
- Z. Varga, H. Jia, B. Sakmann, A. Konnerth, *Proc. Natl. Acad. Sci. U.S.A.* **108**, 15420 (2011).
- N. Takahashi, T. Sasaki, W. Matsumoto, N. Matsuki, Y. Ikegaya, *Proc. Natl. Acad. Sci. U.S.A.* **107**, 10244 (2010).
- A. K. Lee, M. A. Wilson, *Neuron* **36**, 1183 (2002).
- T. Kleindienst, J. Winnubst, C. Roth-Alpermann, T. Bonhoeffer, C. Lohmann, *Neuron* **72**, 1012 (2011).
- H. Makino, R. Malinow, *Neuron* **72**, 1001 (2011).

Acknowledgments: The authors are grateful to K. Morita (University of Tokyo) for his comments on the manuscript. This work was partly supported by Grants-in-Aid for Science Research from the Ministry of Education, Culture, Sports, Science and Technology of Japan (nos. 21220006, 22115003, 23115504, and 23800019); the Strategic Research Program for Brain Sciences (development of biomarker candidates for social behavior); and by the Funding Program for Next Generation World-Leading Researchers (grant LS023).

Supporting Online Material

www.sciencemag.org/cgi/content/full/335/6066/353/DC1
Materials and Methods
Figs. S1 to S15
References
Movie S1

27 June 2011; accepted 2 December 2011
10.1126/science.1210362

Locally Synchronized Synaptic Inputs

N. Takahashi, K. Kitamura, N. Matsuo, M. Mayford, M. Kano, N. Matsuki, Y. Ikegaya

Contents

1. Methods

- 1.1 Slice culture preparation
- 1.2 Electrophysiology
- 1.3 *Ex vivo* calcium imaging of synaptic inputs
- 1.4 *Ex vivo* Calcium imaging of neuronal outputs
- 1.5 *In vivo* calcium imaging of synaptic inputs
- 1.6 Transgenic mouse and behavioral task
- 1.7 Immunohistochemistry
- 1.8 Biocytin reconstruction

2. Supporting Figures and Movie

- Figure S1 Two working hypotheses for the spatial patterns of dendritic inputs from presynaptic cell assemblies
- Figure S2 Dendrites receive spatially biased synchronous inputs
- Figure S3 Calcium elevations in spines serve as reliable reporters of synaptic inputs
- Figure S4 Firing rates of neurons are approximately two times greater than spine activity rates
- Figure S5 Spine activation is spatially clustered on dendrites: reshuffling simulation
- Figure S6 Synaptic inputs are not clustered in fast-spiking parvalbumin-positive interneurons
- Figure S7 Four possible mechanisms that can explain clustered synaptic activation
- Figure S8 Single axo-dendritic proximities have single putative synaptic contacts
- Figure S9 Spine activation is clustered in locally disinhibited dendrites
- Figure S10 Assemblies are sparse over dendritic trees
- Figure S11 Dendritic branches are heterogeneous in assemblies
- Figure S12 Spines that participate in assemblies have large heads
- Figure S13 Chronic blockade of NMDA receptors does not affect synaptic activity
- Figure S14 Clustered synaptic plasticity in behaving adult mice
- Figure S15 A possible mechanism underlying the emergence of assemblies
- Movie S1 Time-lapse confocal imaging of calcium activity from spines

3. References

1. MATERIALS and METHODS

Experiments were performed with the approval of the animal experiment ethics committee at the University of Tokyo (approval number: 19-43) according to the University of Tokyo guidelines for the care and use of laboratory animals.

We report all averaged values as the means \pm S.D. unless otherwise specified.

1.1 Slice culture preparation

Organotypic slice cultures were used for functional spine imaging because the transparency of this tissue allowed optical access to a large number of spines *en masse*. Entorhinal-hippocampal organotypic slices were prepared from 7-d-old Wistar/ST rats (S1). Rat pups were anesthetized by hypothermia and decapitated. The brains were removed and placed in aerated ice-cold Gey's balanced salt solution supplemented with 25 mM glucose. Horizontal entorhinal-hippocampal slices were cut at a thickness of 300 μ m using a vibratome. The slices were placed on Omnipore membrane filters and incubated in 5% CO₂ at 37°C. The culture medium, which was composed of 50% minimal essential medium, 25% Hanks' balanced salt solution, 25% horse serum, and antibiotics, was changed every 3.5 d. In some experiments, slices were cultivated in the same medium with the addition of 100 μ M L,D-2-amino-5-phosphonopentanoic acid (AP5) from day 0 *in vitro*. Experiments were performed at 12–19 d *in vitro* unless otherwise specified.

1.2 Electrophysiology

An entorhinal-hippocampal slice was placed in a recording chamber and perfused at 30–32°C at a rate of 3–4 ml/min with artificial cerebrospinal fluid (aCSF) consisting of 127 mM NaCl, 26 mM NaHCO₃, 3.5 mM KCl, 1.24 mM KH₂PO₄, 1.0 mM MgSO₄, 1.8–2.0 mM CaCl₂, 10 mM glucose,

and 200 μ M Trolox. For dendrite patching, Alexa Fluor 488 was electroporated into the somata of CA3 pyramidal cells by applying one or two rectangular negative pulses (10 ms, 10–15 V) through a glass pipette (4–6 M Ω) loaded with 1 mM Alexa Fluor 488. The apical dendrites were visualized and targeted under Nipkow-disk confocal control using Alexa Fluor 488-conjugated albumin-coated glass pipettes (14–20 M Ω) (S2) filled with 130 mM K-gluconate, 10 mM KCl, 10 mM HEPES, 10 mM phosphocreatine, 4 mM MgATP, 0.3 mM NaGTP, and 0.2% biocytin. Dendrites were current-clamped at approximately -70 mV (the reversal potential of GABA), and spontaneous excitatory postsynaptic potentials were recorded. For soma patching, whole-cell recordings were made from CA3 pyramidal cells and parvalbumin-positive fast-spiking cells using a MultiClamp 700B amplifier. For pyramidal cells, patch pipettes (4–6 M Ω) were filled with 130 mM CsMeSO₄, 10 mM CsCl, 10 mM HEPES, 10 mM phosphocreatine, 4 mM MgATP, 0.3 mM NaGTP, 0.2% biocytin, and 200 μ M Fluo-5F. For parvalbumin-positive cells, the same pipettes were filled with 130 mM K-gluconate, 10 mM KCl, 10 mM HEPES, 10 mM phosphocreatine, 4 mM MgATP, 0.3 mM NaGTP, 0.2% biocytin, and 200 μ M Fluo-5F. Signals were low-pass filtered at 2 kHz and digitized at 20 kHz. Spontaneous and miniature excitatory postsynaptic currents (EPSCs) were recorded at -70 mV. Miniature EPSCs were recorded in the presence of 1 μ M TTX and 50 μ M picrotoxin. In some experiments, electrical field stimulation (50 μ s, 3–6 V) was applied every 5 s using monopolar tungsten electrodes to generate synchronous inputs to a patched neuron. Electrodes were placed in the CA3 striatum radiatum at least 300 μ m away from the imaged dendrites of the patched cells. During stimulation, a low concentration (2 nM) of TTX was perfused to reduce the spontaneous firing of surrounding neurons.

1.3 *Ex vivo* calcium imaging of synaptic inputs

Pyramidal cells and interneurons were voltage-clamped at -30 mV and -70 mV, respectively, to facilitate channel currents mediated by NMDA receptors and calcium-permeable AMPA receptors. Images were acquired at 10–20 frames/s for 120–300 s using a Nipkow-disk confocal unit, a back-illuminated EM-CCD camera (512×512 pixels), and a water-immersion objective lens ($40\times$, 0.80 NA). Fluorophores were excited at 488 nm (about 0.8 mW) and visualized with a 507-nm long-pass emission filter. To avoid a space clamp problem, only spines located within $200 \mu\text{m}$ of the soma were monitored. For each spine, the fluorescence change $\Delta F/F$ was calculated as $(F_t - F_0)/F_0$ where F_t is the fluorescence intensity at frame time t and F_0 is the baseline. Input timings were determined as the onset of individual Ca^{2+} transients with an automatic machine-learning algorithm (S3). To examine the developmental effect of assembly formation, slice cultures were used at 3–4 d *in vitro*. Because these immature networks showed a low level of spontaneous activity, the K^+ concentration was increased to 4.0 mM. Under these conditions, CA3 pyramidal cells occasionally exhibited calcium elevations in their dendritic shafts, which were irrelevant to synaptic inputs and not considered in the data analysis. In some experiments, 1 mM AP5 or 1 mM picrotoxin was locally pressure-applied together with $40 \mu\text{M}$ Alexa Fluor 594 through a patch pipette placed near the imaged dendrites. The spatial spread of the ejected solution was monitored based on Alexa Fluor 594 fluorescence and set to be restricted within $100 \mu\text{m}$ (S4). The head width (φ) of each spine was measured in the Z plane that gave the maximal spine area of the Z-series confocal planes (0.2 to $0.4\text{-}\mu\text{m}$ steps), and the spine head size was calculated as $4\pi(\varphi/2)^3/3$.

1.4 *Ex vivo* calcium imaging of neuronal outputs

For calcium imaging of CA3 neurons, a glass pipette (4–6 M Ω) for dye loading was filled with aCSF that consisted of 100 μ M OGB1-AM, 15% Pluronic F-127, and 10% DMSO. The tip of the pipette was inserted into the stratum pyramidale, and the dye solution was injected by manually controlling a 1-ml syringe pressurizer (10–30 hPa for 1–3 min). Images were acquired at 100 frames/s with a Nipkow-disk confocal unit, a high-speed back-illuminated CCD camera, a water-immersion objective lens (16 \times , 0.80 NA, Nikon, Tokyo, Japan), and Solis software (Andor). Fluorophores were excited at 488 nm and visualized with a 507 nm long-pass emission filter. In each cell body, the fluorescence change $\Delta F/F$ was calculated as $(F_t - F_0)/F_0$ where F_t is the fluorescence intensity at frame time t and F_0 is the baseline. Spike timings were determined as the onset of individual Ca²⁺ transients with an automatic machine-learning algorithm that could accurately detect the timings with zero- or one-frame-jitter errors (S3).

1.5 *In vivo* calcium imaging of synaptic inputs

C57BL/6N mice (P30–35) were anesthetized by 1.5 mg/kg urethane. Depth of anesthesia was monitored regularly by observing whisker movements and the pinch withdrawal reflex of the hindlimb; additional doses of anaesthetic were given as needed. Body temperature was monitored by a rectal temperature probe and maintained at $37 \pm 1^\circ\text{C}$ using a heating pad. After removing the skin, a small craniotomy (2–3 mm in diameter) was performed above the barrel cortex (3 mm lateral to the midline and 1.5 mm posterior to the bregma). The dura was removed and exposed brain surface was subsequently covered by 1.5–2% agarose and coverslip to suppress movement artifact. Whole-cell recordings were made from layer 2/3 pyramidal cells under direct visual

control by shadow-patching method (S5). Patch pipettes (5–7 M Ω) were filled with internal solution contained 135 mM Cs-gluconate, 10 mM HEPES, 3 mM MgATP, 0.3 mM Na₂GTP, 10 mM Na-phosphocreatine, 5 mM QX-314 chloride, 300 μ M Fluo-5F, and 50 μ M Alexa594. During two-photon calcium imaging, neurons were voltage-clamped at -30–0 mV. Calcium imaging was performed using a two-photon microscope with a mode-locked Ti:sapphire laser (wavelength: 810 nm, average power: 5–25 mW) in conjunction with a 25 \times water-immersion objective lens. Fluorescence was divided into green (Fluo-5F) and red (Alexa 594) channels through a dichroic mirror and detected by a pair of photomultiplier tubes. Images were acquired at 6–8 frames/s.

1.6 Transgenic mouse and behavioral task

The GFP-GluR1/c-fos transgenic mice were described previously (S6). Briefly, c-fos-tTA and tetO-GFP-GluR1 transgenes were microinjected into BALB/cByJ and C57BL/6J F2 hybrid embryos and implanted into pseudo-pregnant females. All transgenic mice were maintained as heterozygotes and were backcrossed to C57BL/6J mice. Mice were fed on a Dox diet (40 mg/kg of mouse chow) from the time of weaning (3–4 w old) and were used for experiments at 11–14 w of age. Only males were used for our experiments. Mice were individually housed for 1 w and deprived of Dox for 4 d prior to the experiments. On the experimental day, mice were placed in a novel rectangular chamber and allowed to explore it for 500 s. The mice were subsequently returned to their home cages and treated with a high dose of Dox (6 g/kg) to rapidly suppress additional expression of GFP-GluR1. After 24 h, the brains were sagittally sectioned at a thickness of 100 μ m using a vibratome and fixed with 4% paraformaldehyde (PFA) for 1 h. Without permeabilization, the slices were incubated with a rabbit anti-GFP antibody at 4°C overnight and

were incubated with an Alexa Fluor 488-conjugated goat anti-rabbit secondary antibody at 4°C overnight. Micropipettes were coated with DiI (1,1'-dioctadecyl-3,3,3',3'-tetramethylindocarbocyanine perchlorate) dissolved in ethanol at 10 mg/ml. The tip of the DiI-coated micropipette was inserted at several positions in the CA1 pyramidal cell layer of fixed slices using a micromanipulator. Next, slices were placed in phosphate-buffered saline (PBS) at 4°C for 3–4 d to allow the DiI to spread throughout the dendritic arbor. For each spine, the volume-normalized expression level of GFP was calculated as $F_{\text{GFP}}/F_{\text{DiI}}$ where F_{GFP} and F_{DiI} were the mean fluorescence of GFP and DiI in the spine. Spines with GFP levels that exceeded $1 \times \text{SD}$ of the mean GFP level across all spines were defined as GFP-positive spines.

1.7 Immunohistochemistry

After recording, the slices were fixed with 4% PFA in PBS at 4°C overnight. The slices were blocked with 5% normal goat serum and 0.1% Triton X-100 in PBS at room temperature for 15 min and were incubated in primary anti-parvalbumin rabbit IgG antibody at 4°C overnight. Following incubation in the primary antibody, the slices were rinsed and treated with an Alexa Fluor 594-conjugated goat anti-rabbit secondary antibody at room temperature for 5 h.

1.8 Biocytin reconstruction

To enhance the probability of synaptic transmission, the extracellular solution of 2.5 mM K^+ , 2.4 mM Ca^{2+} , and 4.0 mM Mg^{2+} was used for dual patch-clamp recordings to search synaptically connected neuron pairs. For visualization of these neurons, the slices were fixed in 4% PFA and

0.05% glutaraldehyde in PBS at 4°C overnight. After the PBS washes, the slices were incubated with 0.3% H₂O₂ in PBS for 30 min. After permeabilization in 0.2% Triton X-100 in PBS for 1 h, the slices were processed with an ABC reagent at 4°C overnight. The slices were washed in PBS, equilibrated with Tris-buffered saline (0.05 M; pH 7.5) and developed with 0.0003% H₂O₂, 0.02% diaminobenzidine and 10 mM (NH₄)₂Ni(SO₄)₂ in Tris-buffered saline.

2. Supporting Figures and Video

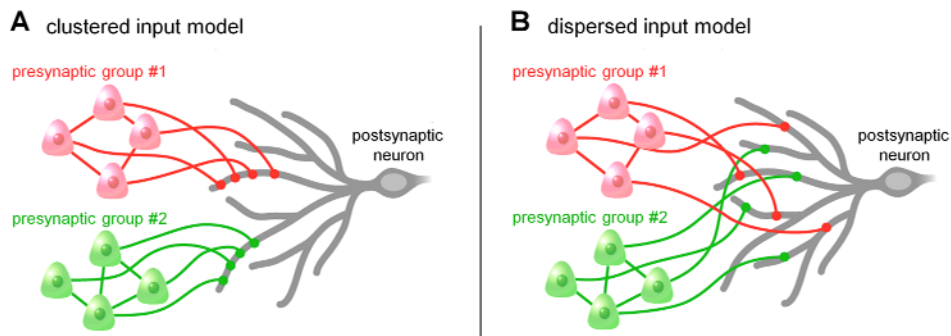


Figure S1 Two working hypotheses for the spatial patterns of dendritic inputs from presynaptic cell assemblies. In the clustered input model (A), afferents from synchronous neuron group 1 (or 2) converge onto a small segment of a postsynaptic neuronal dendrite; in the dispersed input model (B), the afferent terminals diverge over the dendritic trees.

Note: The present work supports the clustered input model.

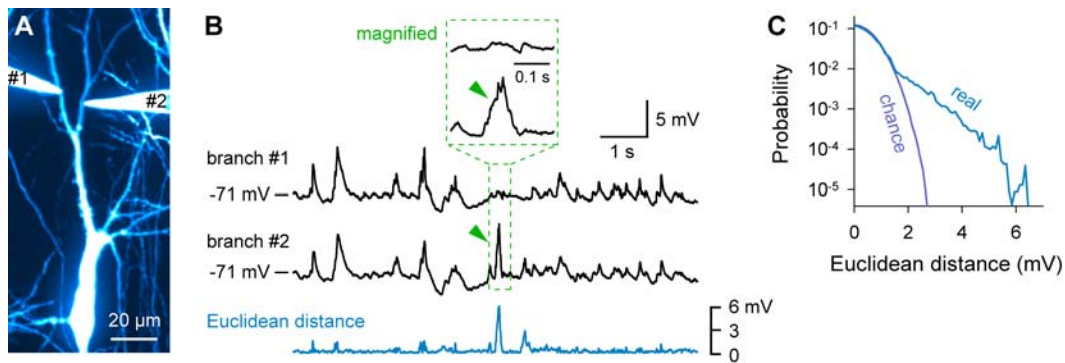


Figure S2 Dendrites receive spatially biased synchronous inputs. (A) A stacked confocal image of a dual-patched CA3 pyramidal cell. Alexa Fluor 594 was electrophoretically injected from the soma, and the visualized dendritic trees were targeted for current-clamp recording using fluorophore-coated glass pipettes (S2). CA3 pyramidal cells are suitable for dual dendritic patching because their thick apical dendrites are usually bifurcated as shown in this photograph. (B) Typical traces of spontaneous fluctuations in membrane potentials simultaneously recorded from two dendrites (black traces). Dynamics of membrane potentials were largely similar between the dendrites, but large postsynaptic potentials occasionally occurred in only one dendrite (arrowhead), which suggests spatially biased synchronous synaptic inputs. The bottom blue trace indicates the time change in the Euclidean distance between two membrane potentials (10-ms bins). (C) The Euclidean distance showed a heavily tailed distribution with a small fraction of time spent for large distances (real, for 3 min). As a control, a Poisson distribution was obtained by assuming that the Euclidean distance fluctuated randomly due to background noise (chance). The noise level was obtained in the same dataset. The real distribution was more heavily tailed than the Poisson distribution ($p < 0.01$, Kolmogorov-Smirnov test), indicating that spatially biased synchronous inputs occurred more frequently than would be expected by chance. Similar results were obtained in all three of the recorded neurons.

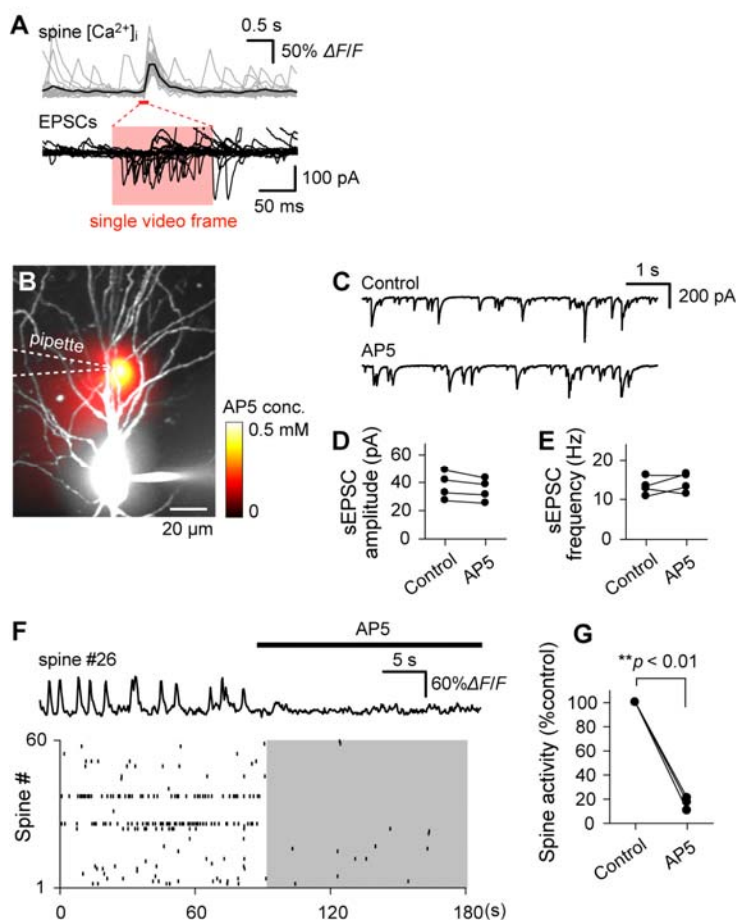


Figure S3 Calcium elevations in spines work as reliable reporters of synaptic inputs. (A) The timing of spine calcium events (top) is associated with the EPSC timing (bottom). Twenty raw calcium traces (gray) and their mean trace (black) recorded from a spine are shown with the patch-clamp traces corresponding to time. The red-colored period indicates the video frame (100 ms) that showed the onset of the calcium events. (B-G) Blocking NMDA receptor activity abolished spontaneous calcium spine activity. (B) AP5 (1 mM) was locally applied to the observed dendritic trees through a puffing micropipette. The AP5 gradient was defined by the fluorescence of Alexa 594 from the same puffing micropipette. (C) Spontaneous synaptic activity before and after the local application of AP5. (D,E) The amplitude and frequency of the sEPSCs were not changed by AP5 application ($p > 0.1$, paired t -test, $n = 4$ neurons for each). (F) A representative calcium trace (top) and raster plot (bottom) show that AP5 application decreased the frequency of the spine calcium transients. The period of AP5 application is shown by a black line (top) and a gray area (bottom). (G) The frequency of calcium events in the spines was reduced by AP5 application ($p < 0.01$, paired t -test, $n = 4$ videos from 4 neurons).

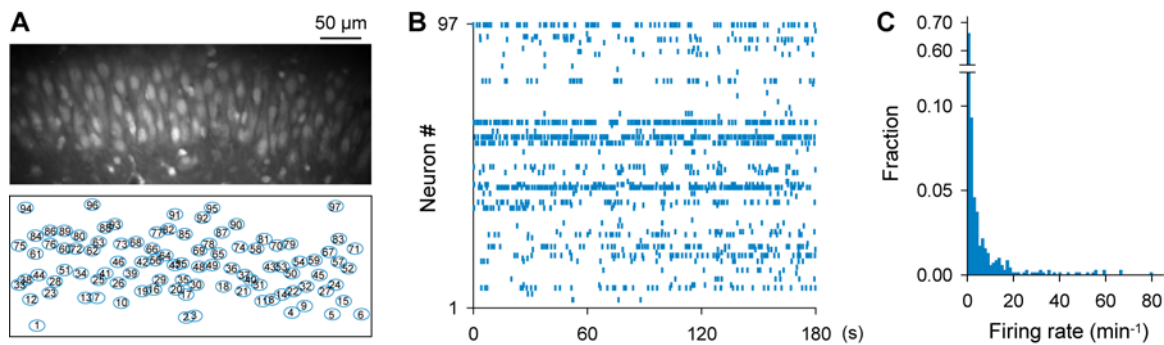


Figure S4 Firing rates of neurons are approximately two times greater than spine activity rates. (A) Representative data of multi-neuron calcium imaging from the CA3 stratum pyramidale of a slice culture under the same experimental conditions, including temperature and extracellular ionic concentrations, as those used for the spine calcium imaging. (A) A raw confocal image; Left bottom: locations of 97 neurons. (B) A raster plot of calcium events of the 97 neurons. (C) Distribution of the frequency of spontaneous calcium activity of individual CA3 neurons.

Note: The mean \pm S.D. of the event frequency from 699 neurons was $3.6 \pm 10.3 \text{ min}^{-1}$. Because the activity rate of 1,084 spines was $1.5 \pm 3.8 \text{ min}^{-1}$ (Fig. 1E,G), the frequency of spine events was 58% lower than that of the soma events. Conversely, the rate of transmitter release or action potential propagation failure (S7) during the patch-clamp recordings from synaptically connected pairs of CA3 pyramidal neurons in the slice cultures is approximately 50% (S8). Therefore, the activity frequency of the spines was consistent with the firing rates of the neurons, which indicates that our spine imaging captured the majority of the synaptic inputs (S9).

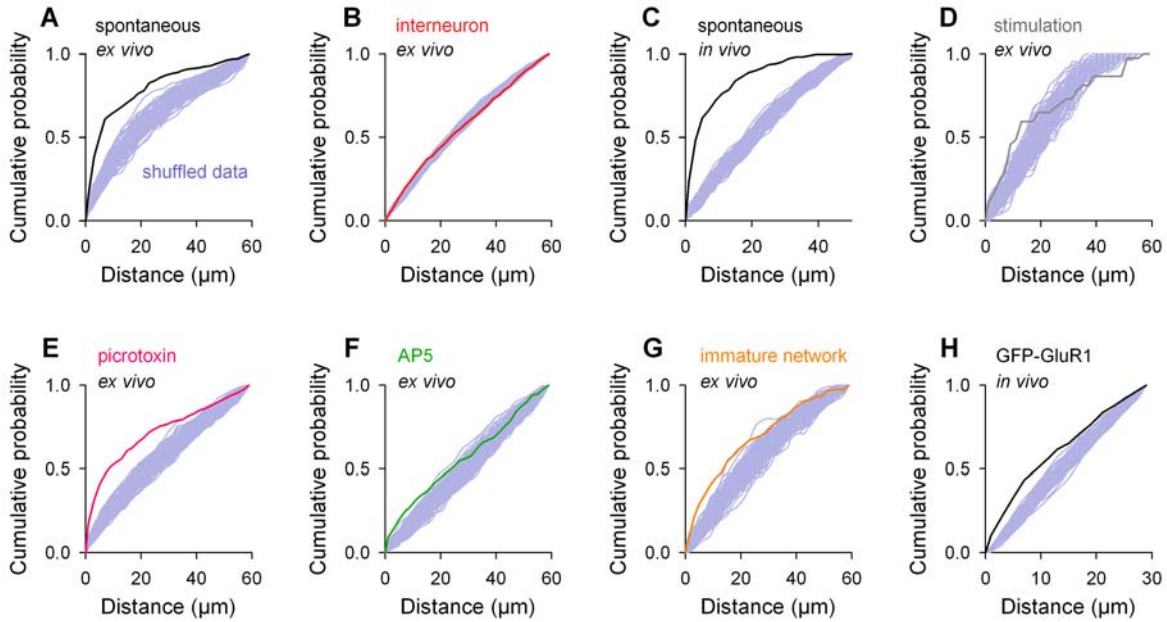


Figure S5 Spine activation is spatially clustered on dendrites: reshuffling simulation. The distribution of the path length between two coactivated spines was compared to that in surrogates, which was obtained by a random shuffling of the spine identity in each dataset. In this shuffling method, only the temporal patterns of calcium activity were exchanged between spines. Thus, the location of individual spines and the temporal and population modulations in the overall spine activity were completely preserved. This tightly restricted data shuffling was designed to avoid a false-positive overestimation of the significance level, which may occur in a simple Monte-Carlo simulation. For each dataset, 100 surrogates were generated. The cumulative probability of the path distances between all possible pairs of synchronized spines was compared between the original datasets (thick lines) and their surrogates (thin gray lines). (A) Spontaneous spine activity of CA3 pyramidal cells in control slices after 12–19 d of culture *in vitro*. (B) Spontaneous dendrite activity of CA3 fast-spiking parvalbumin-positive interneurons in control slices after 12–19 d of culture *in vitro*. (C) Spontaneous spine activity of layer 2/3 pyramidal cells in the somatosensory cortex of anesthetized mice. (D) Stimulation-evoked spine activity of CA3 pyramidal cells in control slices after 12–19 d of culture *in vitro*. (E) Spontaneous spine activity following application of picrotoxin to the dendrites of CA3 pyramidal cells in the control slices after 12–19 d of culture *in vitro*. (F) Spontaneous spine activity of CA3 pyramidal cells in slices cultured in the present of AP5 for 12–19 d. (G) Spontaneous spine activity of CA3 pyramidal cells in control slices after 3–4 d of culture *in vitro*. (H) GFP-positive spines of CA1 pyramidal cells *in vivo*.

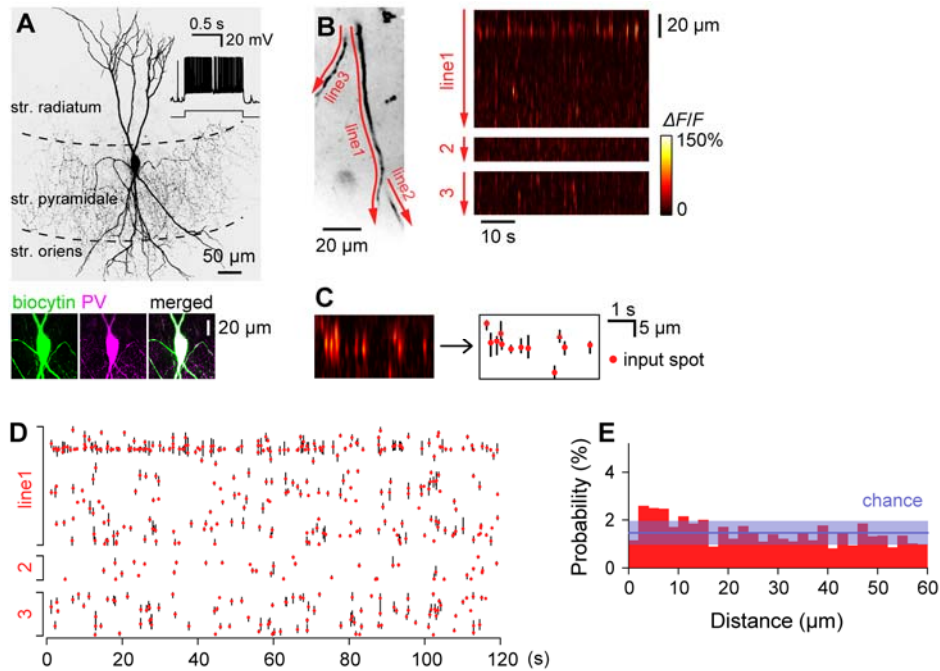


Figure S6 Synaptic inputs are not clustered in fast-spiking parvalbumin-positive interneurons. (A) Biocytin reconstruction of a recorded interneuron. The cell type was identified by its non-adaptive spiking pattern (inset) and immunohistochemical staining for intra-pipette biocytin (green) and parvalbumin (PV, magenta; bottom). (B) Three dendritic branches were confocally time-lapse imaged, and the video was line-scanned *post hoc*. (C) Detection of synaptic input loci from spontaneous calcium activity. Each red dot represents the site (spot) that gave the strongest fluorescent signal in a calcium event, and its subsidiary line shows the region of a significant fluorescence increase. (D) Representative raster plot of calcium events. (E) Probability of observing co-activated calcium spots as a function of the path distance between the coactivated spots. Spatial clustering of calcium activity was not observed ($|Z| \geq 0.63$, $p \leq 0.53$; $n = 11$ videos from 8 neurons). The same conclusion was drawn from the reshuffling simulation (Fig. S5B).

Note: Inhibitory interneurons exhibited highly localized calcium activity in their aspiny dendrites, as reported previously (S10, 11). Because they are highly excitable and can fire in response to a single excitatory input (S12), they may not require dendritic integration via synaptic clustering. For another type of interneuron, see ref. S10.

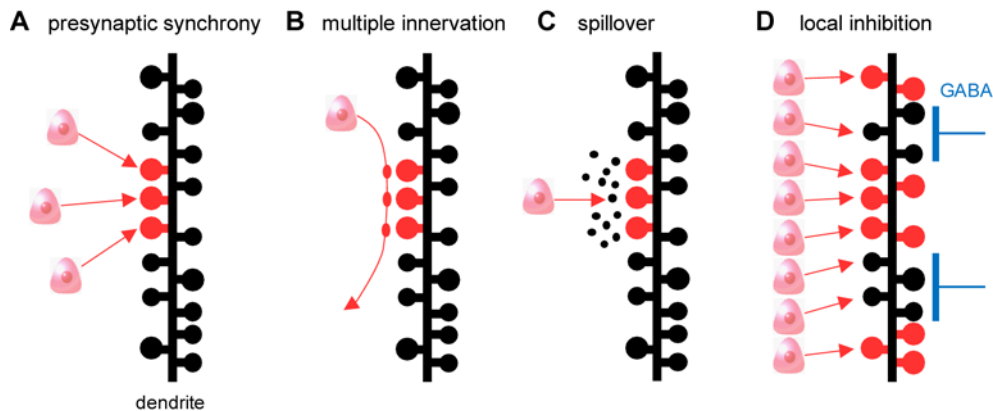


Figure S7 Four possible mechanisms that can explain spatially clustered synaptic activation. (A) A population of spontaneously synchronized presynaptic neurons (cell assembly) project convergently to a narrow segment of a postsynaptic dendrite and simultaneously activates the adjacent spines. (B) A single presynaptic axon makes multiple “*en passant*” synapses with a narrow dendritic segment of a single neuron (S13) and simultaneously activates adjacent spines. (C) Diffusible molecules, such as glutamate, released from a single synapse spread to neighboring spines (S14) and synchronize the activity of adjacent spines. (D) Broad excitatory synaptic inputs are spatially segregated by local inhibitory inputs.

Note: To discriminate these four mechanisms, we carried out three series of analyses (i-iii) as follows. (i) Electrical stimulation. Field stimulation of CA3 stratum radiatum evoked massive activation of fibers passing near the stimulating electrode tip and mimicked network synchronization. This synchronization consisted of artificially selected neurons and did not reflect intrinsically occurring cell assembly dynamics. If mechanism B or C is true, even stimulation-evoked synchronization would produce spatially clustered spine activity. In fact, stimulation did not evoke clustered activity (Fig. 2A bottom, S5D). Thus, mechanisms B and C are unlikely. (ii) Anatomical reconstruction of synaptic contacts. The site where an axon fiber approaches a dendritic spine (an axo-dendritic proximity) is a candidate location for where the axon makes synaptic contacts. Biocytin was injected into synaptically connected neurons and *post hoc* labeled with avidin and diaminobenzidine, and the neuronal morphology was inspected by optical microscopy. We found that only 7.7% of the analyzed synapses had multiple contact sites (Fig. S8). Given that 31.5% of the spines participated in assemblers, mechanism B cannot fully explain the assembler dynamics. (iii) Local blocking of GABAergic inhibitory inputs. Picrotoxin was locally applied to the imaged dendrites to block inhibitory transmission. Even under disinhibited conditions, clustered spine activation was intact (Fig. S5E, S9). This result excludes mechanism D. Note that mechanism D is also inconsistent with the sparseness of assemblers; assemblers usually appeared alone (Fig. S10A) and were unlikely to result from segregation by inhibition.

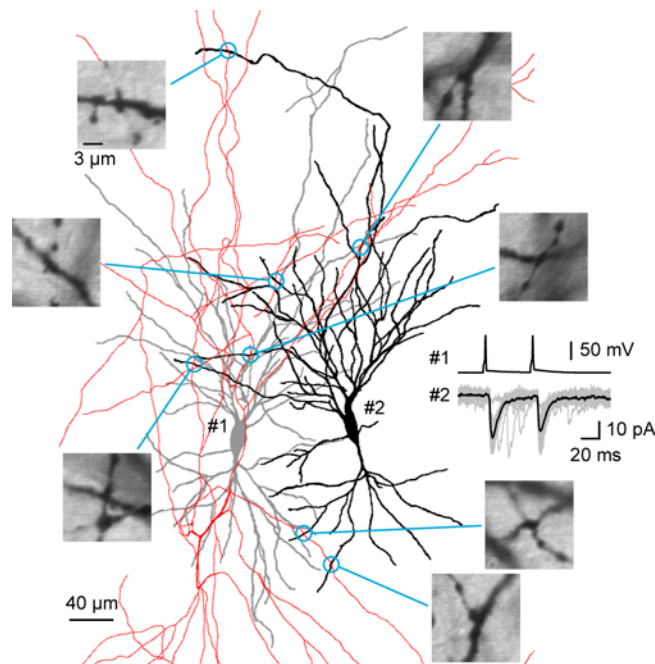


Figure S8 Single axo-dendritic proximities have single putative synaptic contacts. A pair of synaptically connected CA3 pyramidal cells were filled with biocytin and reconstructed using a camera lucida. Circles represent axo-dendritic proximities, *i.e.*, candidates of synaptic contacts (S15), and these regions are shown in high-magnification photographs. Traces are unitary EPSCs recorded by dual patch-clamping from neurons 1 (pre) and 2 (post). The reconstruction was repeated for axons from 12 neurons, and 51 of 55 (92.7%) proximities had single contact sites, whereas other proximities (7.3%) had two or three contact sites. Given that 31.5% of the spines participated in assemblets, multiple synapses of single axons onto small dendritic segments, if there are any, are unlikely to contribute significantly to the functional synaptic clustering observed in spine calcium imaging.

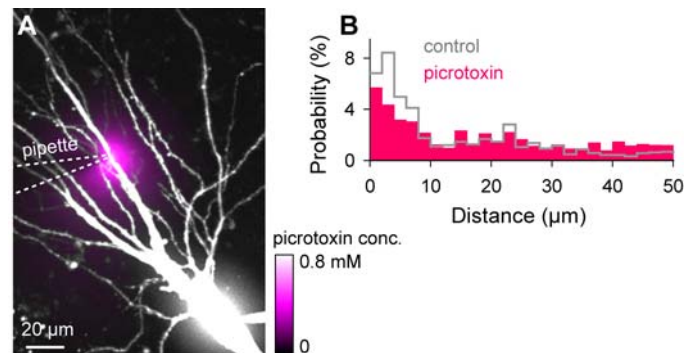


Figure S9 Spine activation is clustered in locally disinhibited dendrites. (A) Dendrites of CA3 pyramidal cells were treated with a local puffing of 1 mM picotoxin, and the spines were imaged in the area where the Alexa-estimated concentration of picotoxin was greater than 100 μM. (B) The probability of observing co-activated spines ($|Z| \geq 3.97$, $p \leq 7.2 \times 10^{-5}$; $n = 8$ videos from 8 neurons). The control is the same as in Fig. 2A. The Kolmogorov-Smirnov test indicated no significant difference between control and picotoxin-treated dendrites ($p > 0.1$). The same conclusion was obtained from the reshuffling simulation (Fig. S5E).

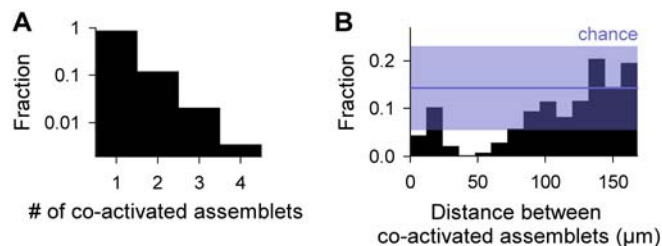


Figure S10 Assemblies are sparse over dendritic trees. (A) Distribution of the number of assemblies coactivated within a time window of 100 ms. (B) Distribution of the path distance between any pair of synchronized assemblies. The chance level and its 95% confidence interval (purple) were estimated from the distribution at distances of more than 100 μm . Coactivation seemed to be rare when assemblies were within 70 μm of one another.

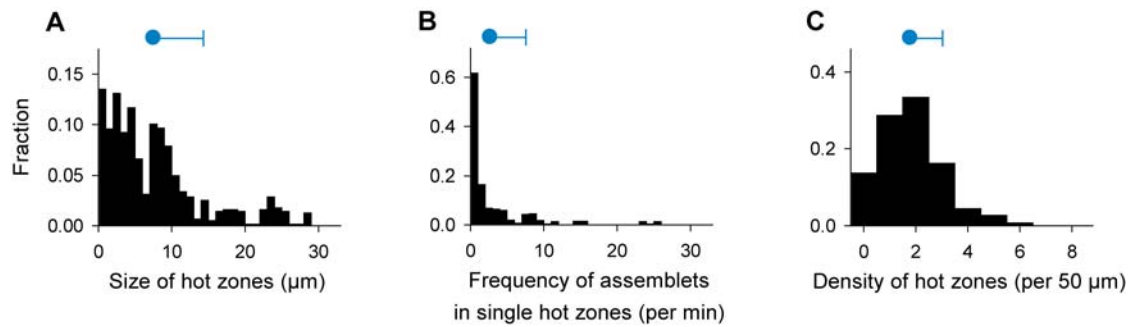


Figure S11 Dendritic branches are heterogeneous in assembles. (A) Distribution of the path length of single hot zones. Mean \pm S.D. = $7.7 \pm 6.7 \mu\text{m}$, CV = 0.88, $n = 79$ hot zones in 11 neurons. (B) Distribution of the number of assemblies emitted by single hot zones per minute. Mean \pm S.D. = $2.7 \pm 4.8 \text{ min}^{-1}$, CV = 1.76. (C) Distribution of the density of hot zones per 50 μm of dendritic length. Mean \pm S.D. = 1.8 ± 1.2 , CV = 0.68.

Note: All of these parameters varied greatly from dataset to dataset, which suggests that hot zones are non-uniform over the dendritic trees.

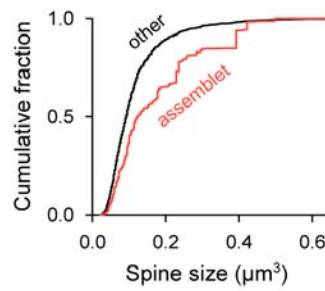


Figure S12 Spines that participate in assemblies have large heads. The cumulative distribution of the head sizes of spines that participated in at least one assembly (assembly, $n = 341$ spines) was significantly rightwarded compared to spines that were not involved in an assembly (other, $n = 743$ spines; $p < 0.01$, Kolmogorov-Smirnov test).

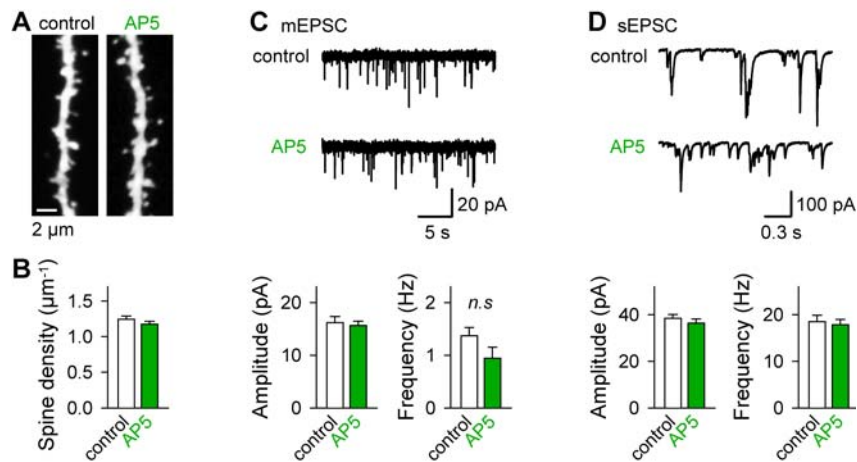


Figure S13 Chronic blockade of NMDA receptors does not affect synaptic activity. Slices were cultivated in the chronic presence of 100 μ M AP5 for 12–19 d *in vitro*. (A) Biocytin visualization of spines in the basal dendrites of control or AP5-treated CA3 pyramidal cells. (B) Spine density was not different between control and AP5-treated pyramidal cells (control, $n = 18$ branches from 9 cells; AP5, $n = 21$ branches from 10 cells). (C, D) Neither the amplitude nor the frequency of miniature EPSCs (C; mEPSC, $n = 11$ and 12 cells, respectively) or spontaneous EPSCs (D; sEPSC, $n = 25$ cells each) was different between the control and AP5-treated pyramidal cells. Data are the means \pm S.E.M.

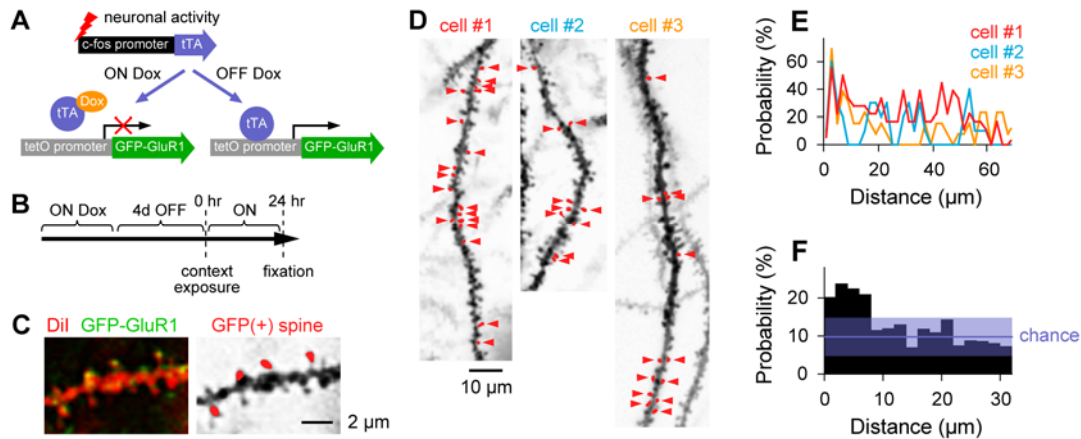


Figure S14 Clustered synaptic plasticity in behaving adult mice. (A) Schematic representation of the transgenic mouse system. GFP-fused GluR1 AMPA receptor subunit (GFP-GluR1) was expressed under control of the *c-fos* promoter (S6). The *c-fos* promoter drives activity-dependent expression of the tetracycline-regulated transactivator (tTA), which, in turn, activates transcription of the tetO promoter-linked GFP-GluR1 in a doxycycline (Dox)-regulated manner. (B) Experimental design. Mice were deprived of Dox for 4 d and were exposed to a novel environment for 500 s. After 24 h, approximately 25% of CA1 pyramidal neurons expressed GFP-GluR1. GFP-positive spines were examined in DiI-labeled CA1 pyramidal cells. (C) Left, representative confocal image of GFP and DiI fluorescence. Right, detection of GFP-positive spines (red) in a DiI-labeled dendrite (black). (D) Representative spatial distribution of GFP-positive spines (red, arrowheads) in the dendrites of three neurons. (E) The probability of observing GFP-positive spines around a given GFP-positive spine in the three cells shown in D. (F) The averaged probability of observing GFP-positive spines in 19 neurons. The chance level and its 95% confidence intervals were obtained from the distribution of distances of more than 10 μm . GFP-positive spines were clustered within 8 μm of one another ($|Z| \geq 4.02$, $p \leq 5.7 \times 10^{-5}$; Fig. S5H; $n = 19$ neurons).

Note: Newly synthesized AMPA receptors are preferentially inserted into previously activated spines and contribute to long-term potentiation. Therefore, we used GFP-GluR1 to probe a part of spines that underwent long-term potentiation.

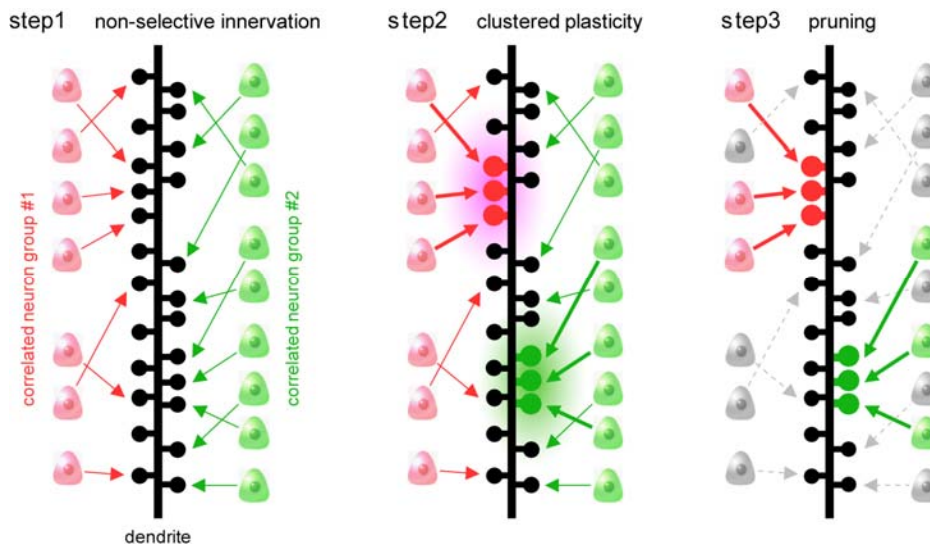


Figure S15 A possible mechanism underlying the emergence of assemblies. Step 1: Individual neurons in groups of synchronized neurons (cell assemblies 1 and 2) make synapses with postsynaptic dendrites in a spatially non-selective manner (non-selective innervation). Step 2: NMDA-dependent long-term potentiation occurs simultaneously in spines that receive synchronized inputs in spatially narrow dendritic regions (clustered plasticity), inducing spine enlargement (S16). Step 3: Synapses that did not exhibit long-term potentiation are weakened or eliminated (pruning). During this network-wide reorganization of synaptic competition, convergently synchronized synapses become predominant.

Note: This model was inspired by the concepts proposed by Govindarajan et al. (S17), DeBello (S18), and Larkum and Nevian (S19). Clustered plasticity may be induced by a synchronous input-induced massive depolarization of a small dendritic segment and/or by intracellular diffusion of plasticity-associated molecules to nearby spines (S20-24).

Movie S1 Time-lapse confocal imaging of calcium activity from spines. A neuron was loaded with Fluo-5F. The changes in the fluorescent signal are shown in a pseudo-color scale and superimposed onto a time-averaged Fluo-5F image.

3. References

- S1. R. Koyama *et al.*, A low-cost method for brain slice cultures. *J Pharmacol Sci* **104**, 191 (2007).
- S2. D. Ishikawa *et al.*, Fluorescent pipettes for optically targeted patch-clamp recordings. *Neural Netw* **23**, 669 (2010).
- S3. T. Sasaki, N. Takahashi, N. Matsuki, Y. Ikegaya, Fast and accurate detection of action potentials from somatic calcium fluctuations. *J Neurophysiol* **100**, 1668 (2008).
- S4. T. Sasaki, N. Matsuki, Y. Ikegaya, Action-potential modulation during axonal conduction. *Science* **331**, 599 (2011).
- S5. K. Kitamura, B. Judkewitz, M. Kano, W. Denk, M. Hausser, Targeted patch-clamp recordings and single-cell electroporation of unlabeled neurons in vivo. *Nat Methods* **5**, 61 (2008).
- S6. N. Matsuo, L. Reijmers, M. Mayford, Spine-type-specific recruitment of newly synthesized AMPA receptors with learning. *Science* **319**, 1104 (2008).
- S7. D. Debanne, N. C. Guerineau, B. H. Gähwiler, S. M. Thompson, Action-potential propagation gated by an axonal I_A -like K^+ conductance in hippocampus. *Nature* **389**, 286 (1997).
- S8. J. M. Montgomery, P. Pavlidis, D. V. Madison, Pair recordings reveal all-silent synaptic connections and the postsynaptic expression of long-term potentiation. *Neuron* **29**, 691 (2001).
- S9. R. Enoki, Y. L. Hu, D. Hamilton, A. Fine, Expression of long-term plasticity at individual synapses in hippocampus is graded, bidirectional, and mainly presynaptic: optical quantal analysis. *Neuron* **62**, 242 (2009).
- S10. J. H. Goldberg, R. Yuste, G. Tamas, Ca^{2+} imaging of mouse neocortical interneurone dendrites: contribution of Ca^{2+} -permeable AMPA and NMDA receptors to subthreshold Ca^{2+} dynamics. *J Physiol* **551**, 67 (2003).
- S11. G. Katona *et al.*, Roller Coaster Scanning reveals spontaneous triggering of dendritic spikes in CA1 interneurons. *Proc Natl Acad Sci U S A*, in press (2011).
- S12. M. Galarreta, S. Hestrin, Spike transmission and synchrony detection in networks of GABAergic interneurons. *Science* **292**, 2295 (2001).
- S13. K. E. Sorra, K. M. Harris, Occurrence and three-dimensional structure of multiple synapses between individual radiatum axons and their target pyramidal cells in hippocampal area CA1. *J Neurosci* **13**, 3736 (1993).

- S14. D. M. Kullmann, F. Asztely, Extrasynaptic glutamate spillover in the hippocampus: evidence and implications. *Trends Neurosci* **21**, 8 (1998).
- S15. Y. Mishchenko *et al.*, Ultrastructural analysis of hippocampal neuropil from the connectomics perspective. *Neuron* **67**, 1009 (2010).
- S16. M. Matsuzaki, N. Honkura, G. C. Ellis-Davies, H. Kasai, Structural basis of long-term potentiation in single dendritic spines. *Nature* **429**, 761 (2004).
- S17. A. Govindarajan, R. J. Kelleher, S. Tonegawa, A clustered plasticity model of long-term memory engrams. *Nat Rev Neurosci* **7**, 575 (2006).
- S18. W. M. DeBello, Micro-rewiring as a substrate for learning. *Trends Neurosci* **31**, 577 (2008).
- S19. M. E. Larkum, T. Nevian, Synaptic clustering by dendritic signalling mechanisms. *Curr Opin Neurobiol* **18**, 321 (2008).
- S20. C. D. Harvey, K. Svoboda, Locally dynamic synaptic learning rules in pyramidal neuron dendrites. *Nature* **450**, 1195 (2007).
- S21. A. Losonczy, J. K. Makara, J. C. Magee, Compartmentalized dendritic plasticity and input feature storage in neurons. *Nature* **452**, 436 (2008).
- S22. C. D. Harvey, R. Yasuda, H. Zhong, K. Svoboda, The spread of Ras activity triggered by activation of a single dendritic spine. *Science* **321**, 136 (2008).
- S23. A. Govindarajan, I. Israely, S. Y. Huang, S. Tonegawa, The dendritic branch is the preferred integrative unit for protein synthesis-dependent LTP. *Neuron* **69**, 132 (2011).
- S24. H. Murakoshi, H. Wang, R. Yasuda, Local, persistent activation of Rho GTPases during plasticity of single dendritic spines. *Nature* **472**, 100 (2011).